

1 Multilayer-HySEA model validation for landslide  
2 generated tsunamis. Part I Rigid slides

3 Jorge Macías\*, Cipriano Escalante, Manuel J. Castro

4 *Departamento de Análisis Matemático, Estadística e Investigación Operativa y Matemática*  
5 *Aplicada, Facultad de Ciencias, Universidad de Málaga, 29080-Málaga*

---

6 **Abstract**

7 This paper is devoted to benchmarking the Multilayer-HySEA model using lab-  
8 oratory experimental data for landslide-generated tsunamis. This article deals  
9 with rigid slides and the second part, in a companion paper, addresses granular  
10 slides. The US National Tsunami Hazard and Mitigation Program (NTHMP)  
11 has proposed the experimental data used and established for the NTHMP Land-  
12 slide Benchmark Workshop, held in January 2017 at Galveston (Texas). The  
13 first three benchmark problems proposed in this workshop deal with rigid slides.  
14 Rigid slides must be simulated as a moving bottom topography and, therefore,  
15 they must be modelled as a prescribed boundary condition. These three bench-  
16 marks are used here to validate the Multilayer-HySEA model. This new HySEA  
17 model consists of an efficient hybrid finite-volume/finite-difference implementa-  
18 tion on GPU architectures of a non-hydrostatic multilayer model. A brief de-  
19 scription of model equations, dispersive properties, and the numerical scheme  
20 is included. The benchmarks are described and the numerical results compared  
21 against the lab-measured data for each of them. The specific aim is to validate  
22 this new code for tsunamis generated by rigid slides. Nevertheless, the over-  
23 all objective of the current benchmarking effort is to produce a ready-to-use  
24 numerical tool for real-world landslide generated tsunami hazard assessment.  
25 This tool has already been used to reproduce the Port Valdez Alaska 1964 and  
26 Stromboli Italy 2002 events.

27 *Keywords:* Multilayer-HySEA model, tsunamis, rigid slides, model  
28 benchmarking, landslide-generated tsunamis, GPU implementation

---

\*Corresponding author  
Preprint submitted to *Natural Hazards and Earth Systems Science*  
Email address: [jmacias@uma.es](mailto:jmacias@uma.es) (Jorge Macías)

30 **1. Introduction**

31 Model development and benchmarking for earthquake-induced tsunamis is a  
32 task addressed in the past and to which much effort and time has been dedicated.  
33 In particular, just to mention a couple of NTHMP efforts, the 2011 Galveston  
34 benchmarking workshop (Horrillo et al., 2015) and the 2015 Portland workshop  
35 for tsunami currents (Lynett et al., 2017) both focused on these topics. However,  
36 both model development and benchmarking efforts have advanced at a slower  
37 pace for landslide-generated tsunamis. As examples we might mention the 2003  
38 NSF-sponsored landslide tsunami workshop organized in Hawaii and a similar  
39 follow-up workshop on Catalina Island in 2006 (Liu et al., 2008). Since then, no  
40 similar large comprehensive benchmarking workshop has been organized (Kirby  
41 et al., 2018).

42 In its 2019 Strategic Plan, the NTHMP required that all numerical tsu-  
43 nami inundation models to be used in hazard assessment studies in the US  
44 be verified as accurate and consistent through a model benchmarking process.  
45 This mandate was fulfilled in 2011, but only for seismic tsunami sources and to  
46 a limited extent for idealized solid underwater landslides. However, recent work  
47 by various NTHMP states has shown that landslide tsunami hazard may in fact  
48 be greater than seismically-induced hazard and may be also the dominant risk  
49 along significant parts of the US coastline (ten Brink et al., 2014).

50 As a result of this demonstrated gap, a set of candidate benchmarks was pro-  
51 posed to perform the required validation process. The selected benchmarks are  
52 based on a subset of available laboratory data sets for solid slide experiments  
53 and deformable slide experiments and include both submarine and subaerial  
54 slides. In order to complete this list of laboratory data, a benchmark based  
55 on a historic field event (Valdez, AK, 1964) was also chosen. The EDANYA  
56 group ([www.uma.es/edanya](http://www.uma.es/edanya)) from the University of Málaga participated in  
57 the workshop organized at Texas A&M University, Galveston (January 9-11,

58 2017) presenting results for the benchmarking tests with two numerical codes:  
59 Landslide-HySEA and Multilayer-HySEA models. At Galveston, we presented  
60 numerical results for six out of the seven benchmark problems proposed, in-  
61 cluding the field case. The current work presents the numerical results obtained  
62 for the Multilayer-HySEA model in the framework of the validation effort de-  
63 scribed above for the case of rigid slide-generated tsunamis, whereas the bench-  
64 mark problems dealing with granular slides are presented in a companion paper  
65 Macías et al. (2020a). A summary of the results for the field case at Port Valdez  
66 can be found at Macías et al. (2017).

67 Twenty years ago, at the beginning of the century, the challenge of solid  
68 block landslide modelling was taken by a number of researchers (Grilli and  
69 Watts, 1999, 2005; Grilli et al., 2002; Lynett and Liu, 2002; Watts et al., 2003;  
70 Wu, 2004; Watts et al., 2005; Liu et al., 2005) and laboratory experiments were  
71 developed for those cases and for tsunami model benchmarking (Enet and Grilli,  
72 2007) (see also Ataie-Ashtiani and Najafi-Jilani (2008)). The benchmark prob-  
73 lems performed in the current work are based on the laboratory experiments  
74 of Grilli and Watts (2005) for BP1, Enet and Grilli (2007) for BP2, and Wu  
75 (2004); Liu et al. (2005) for BP3. The basic reference for these three bench-  
76 marks, as well as for the three benchmarks related to granular slides and the  
77 Alaska field case (all of them proposed by the NTHMP) is Kirby et al. (2018).  
78 We highly recommend checking this reference for further details on benchmark  
79 descriptions, data provided for performing them, required benchmark items, and  
80 inter-model comparison. Finally, we would like to stress that the ultimate goal  
81 of our current benchmarking effort is to provide the tsunami community with  
82 a NTHMP-approved model for landslide-generated tsunami hazard assessment,  
83 similarly to what we have done with the Tsunami-HySEA model for the case of  
84 earthquake-generated tsunamis (Macías et al., 2017; Macías et al., 2020c,d).

## 85 **2. HySEA models for landslide generated tsunamis**

86 The HySEA (Hyperbolic Systems and Efficient Algorithms) software consists  
87 of a family of geophysical codes based on either single-layer, two-layer stratified  
88 systems or multilayer shallow-water models. HySEA codes<sup>1</sup> have been under  
89 development by the EDANYA Group from UMA (the University of Málaga)  
90 for more than a decade. These codes are in continuous evolution and upgrad-  
91 ing and they are serving to a wider scientific community every day. The first  
92 model we developed dealing with landslide-generated tsunamis consisted of a  
93 stratified two-layer Savage-Hutter shallow-water model -the Landslide-HySEA  
94 model-. It was implemented based on the model described in Fernández et al.  
95 (2008) and was incorporated to the HySEA family. An initial validation of this  
96 code, comparing numerical results with the laboratory experiments of Heller and  
97 Hager (2011) and Fritz et al. (2001) can be found at Sánchez-Linares (2011).  
98 The 2018 numerical simulation of the Lituya Bay 1958 mega-tsunami with real  
99 topo-bathymetric data and encouraging results (González-Vida et al., 2019),  
100 represented a milestone in the verification process of this code. This validation  
101 effort was accomplished under a research contract with PMEL/NOAA. The re-  
102 sult of this project led the NCTR (NOAA Center for Tsunami Research) to  
103 adopt Landslide-HySEA as the numerical code of choice to generate the initial  
104 conditions for the MOST model to be initialized in the case of a landslide-  
105 generated tsunami scenario to be simulated. Further applications of Landslide-  
106 HySEA can be found at de la Asunción et al. (2013), Macías et al. (2015), and  
107 Iglesias (2015).

108 The waves generated in the laboratory tests proposed in the NTHMP se-  
109 lected benchmarks are high frequency and dispersive, and the generated flows  
110 have a complex vertical structure. Therefore, the numerical model used must  
111 be able to reproduce such effects. This makes the two-layer Landslide-HySEA  
112 model unsuitable for reproducing these experimental results as non-hydrostatic

---

<sup>1</sup><https://edanya.uma.es/hysea>

113 effects play an important role and a richer vertical structure is required. To  
114 address these requirements, the Multilayer-HySEA model was very recently im-  
115 plemented, considering a stratified structure in the simulated fluid and including  
116 non-hydrostatic terms. A multilayer model is able to better approximate the  
117 vertical structure of a complex flow than a standard one-layer depth-averaged  
118 model. In particular, increasing the number of layers the linear dispersion re-  
119 lation of the model converges towards the exact dispersion relation from the  
120 Stokes linear theory (see Fernández-Nieto et al. (2018)).

### 121 **3. Model Equations**

122 The Multilayer-HySEA model implements one of the multilayer non-hydro-  
123 static models of the family introduced and described in Fernández-Nieto et al.  
124 (2018) (model  $LDNH_0$ ). The governing equations, that are obtained by a  
125 process of depth-averaging, correspond to a semi-discretization for the vertical  
126 variable of the Euler equations following a standard Galerkin approach. The  
127 total pressure is decomposed into a sum of hydrostatic and non-hydrostatic  
128 pressures and is assumed to have a linear vertical profile. The horizontal and  
129 vertical velocities are assumed to have a constant vertical profile. At the discrete  
130 level on  $z$ , the total pressure matches at the interfaces and velocities satisfy a  
131 discrete jump condition (see Fernández et al. (2008) or Escalante et al. (2018a)).

132 An alternative deduction for this system is performed in Escalante et al.  
133 (2018a) assuming linear vertical profiles for pressure and vertical velocity and  
134 a constant vertical profile for the horizontal velocity, as well as some extra  
135 hypothesis for the case of two layers. The proposed model admits an exact  
136 energy balance and, when the number of layers increases, the linear dispersion  
137 relation of the linear model converges to the same of Airy's theory (Fernández-  
138 Nieto et al., 2018). The model proposed in Fernández-Nieto et al. (2018) can

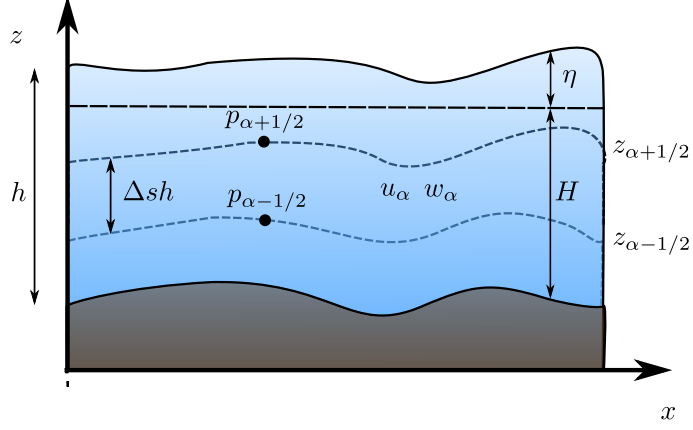


Figure 1: Schematic diagram describing the multilayer system

139 be written in a compact form as:

$$\left\{ \begin{array}{l}
 \partial_t h + \partial_x (h\bar{u}) = 0, \\
 \partial_t (hu_\alpha) + \partial_x \left( hu_\alpha^2 + \frac{1}{2}gh^2 \right) - gh\partial_x H + u_{\alpha+1/2}\Gamma_{\alpha+1/2} - u_{\alpha-1/2}\Gamma_{\alpha-1/2} = \\
 \qquad \qquad \qquad - h(\partial_x p_\alpha + \sigma_\alpha \partial_z p_\alpha) - \tau, \\
 \partial_t (hw_\alpha) + \partial_x (hu_\alpha w_\alpha) + w_{\alpha+1/2}\Gamma_{\alpha+1/2} - w_{\alpha-1/2}\Gamma_{\alpha-1/2} = -h\partial_z p_\alpha, \\
 \partial_x u_{\alpha-1/2} + \sigma_{\alpha-1/2} \partial_z u_{\alpha-1/2} + \partial_z w_{\alpha-1/2} = 0,
 \end{array} \right. \quad (1)$$

140 where, for  $\alpha \in \{1, 2, \dots, L\}$ , the following notation is used:

$$f_{\alpha+1/2} = \frac{1}{2}(f_{\alpha+1} + f_\alpha), \quad \partial_z f_{\alpha+1/2} = \frac{1}{h\Delta s}(f_{\alpha+1} - f_\alpha), \quad (2)$$

141 where  $f$  denotes one of the generic variables of the system, i.e.,  $u$ ,  $w$  and  $p$ , and,

142 finally,

$$\sigma_\alpha = \partial_x (H - h\Delta s(\alpha - 1/2)), \quad \sigma_{\alpha-1/2} = \partial_x (H - h\Delta s(\alpha - 1)). \quad (3)$$

143 Total depth,  $h$ , is split along the vertical axis into  $L \geq 1$  layers and  $\Delta s = 1/L$

144 (see Figure 1). The variables  $u_\alpha$  and  $w_\alpha$  are the depth-averaged velocities in

145 the  $x$  and  $z$  directions, respectively,  $t$  is time and  $g$  is gravitational acceleration.  
 146 The non-hydrostatic pressure at the interface  $z_{\alpha+1/2}$  is denoted by  $p_{\alpha+1/2}$ . The  
 147 water surface elevation measured from the still-water level is  $\eta = h - H$ , where  
 148  $H$  is the water depth when the water is at rest. Finally,  $\tau$  is a friction law term,  
 149 and the terms  $\Gamma_{\alpha+1/2}$  account for the mass transfer across interfaces and are  
 150 defined by

$$\Gamma_{\alpha+1/2} = \sum_{\beta=\alpha+1}^L \partial_x (h \Delta s (u_\beta - \bar{u})), \quad \bar{u} = \sum_{\alpha=1}^L \Delta s u_\alpha \quad (4)$$

151 In order to close the system of equations, the following boundary conditions are  
 152 considered

$$p_{L+1/2} = 0, \quad u_0 = 0, \quad w_0 = -\partial_t H. \quad (5)$$

153 Note that the motion of the bottom surface can be taken into account as a  
 154 boundary condition, imposing  $w_0 \neq 0$ . Therefore, this model can simulate the  
 155 interaction with a slide in the case that the motion of the bottom is prescribed  
 156 by a function, given by a set of data, or simulated by a numerical model. In the  
 157 present study, we are going to consider tests where the motion of the seafloor is  
 158 given by a known function (the solid moving block).

### 159 *3.1. Linear dispersion relation*

160 Some dispersive properties of the system (1) are presented in this subsection,  
 161 in particular, the phase and group velocities, and the linear shoaling. The first  
 162 two properties are related to the propagation of dispersive wave trains and the  
 163 last one to shoaling processes.

164 To obtain such properties, the system (1) is linearised around the water at  
 165 rest steady-state solution. After that, a Stokes-type Fourier analysis is carried  
 166 out looking for first-order planar wave solutions. This method constitutes a  
 167 standard procedure to study systems that model dispersive water waves (see  
 168 Escalante et al. (2018a); Lynett and Liu (2004); Madsen and Sorensen (1992);  
 169 Schäffer and Madsen (1995) and references therein). The phase and group

170 velocities as well as the linear shoaling gradient are, respectively, defined as:

$$C = \omega/k, \quad G = C + k\partial_k C, \quad \frac{\partial_x \eta}{\eta} = -\gamma \frac{\partial_x H}{H}, \quad (6)$$

171 where  $\omega$  denotes the angular frequency,  $k$  the local wave-number and  $H$  the  
172 typical depth.

173 The measured quantities  $C$ ,  $G$  and  $\gamma$  are solely functions of the local wave-  
174 number and the typical depth  $H$ . Thus, one can obtain the so-called linear  
175 dispersion relation of the three measured quantities. From the Airy wave theory,  
176 one can also obtain the corresponding linear dispersion relations that state the  
177 linear theory for the considered quantities (see Schäffer and Madsen (1995) for  
178 the Airy reference formulae). For example, the expression for the phase velocity  
179 from the Airy's theory is

$$C_{Airy} = gH \frac{\tanh(kH)}{kH}. \quad (7)$$

180 The expressions of the phase velocity for the system (1) are given in Table 1  
181 for the non-linear hydrostatic shallow water system (SWE) and the Multilayer-  
182 HySEA (non-hydrostatic) system with  $j \geq 1$  layers (NH-jL). The last two  
183 columns contain  $Er_C(s)$  for  $s = 5$  and  $s = 15$ , where  $Er_C(s)$  represents the  
184 maximum relative error of the phase velocity with respect to the Airy in a  
185 range  $kH \in [0, s]$  in percent, i.e.:

$$Er_C(s) = 100 \cdot \max_{kH \in [0, s]} \left( \frac{|C(kH) - C(kH)_{Airy}|}{|C(kH)_{Airy}|} \right). \quad (8)$$

186 The main goal when deriving dispersive shallow water systems is to get the  
187 most accurate dispersive relations as possible, compared with the Airy wave  
188 theory, without highly increasing the complexity of the system. See Schäffer  
189 and Madsen (1995) for a review on state-of-the-art or a two-layer with improved  
190 dispersive relations in Lynett and Liu (2004), and an enhanced two-layer non-  
191 hydrostatic pressure system in Escalante et al. (2018a). It has been shown  
192 (Fernández-Nieto et al., 2018) that increasing the number of layers leads to the  
193 convergence of the linear dispersion relation of the linear model to the same of  
194 Airy's theory. Figure 2 shows this behavior and highlights the huge discrepancies



Multilayer System – Phase velocity – Errors for $kH$ up to 5 and 15			
Model	Phase velocity	$Er_C(5)$	$Er_C(15)$
(SWE)	$gH$	73.63 %	123.61 %
(NH-1L)	$gH \frac{1}{1 + \frac{1}{4}(kH)^2}$	3.02 %	16.95 %
(NH-2L)	$gH \frac{1 + \frac{(kH)^2}{16}}{1 + \frac{3(kH)^2}{8} + \frac{(kH)^4}{256}}$	0.71 %	10.67 %
(NH-3L)	$\frac{1 + \frac{5(kH)^2}{54} + \frac{(kH)^4}{1296}}{1 + \frac{5(kH)^2}{12} + \frac{5(kH)^4}{432} + \frac{1(kH)^6}{46656}}$	0.31 %	0.62 %
(NH-5L)	$\frac{1 + \frac{3(kH)^2}{25} + \frac{63(kH)^4}{2510^3} + \frac{3(kH)^6}{2510^4} + \frac{(kH)^8}{1010^7}}{1 + \frac{9(kH)^2}{20} + \frac{21(kH)^4}{1010^2} + \frac{21(kH)^6}{1010^4} + \frac{9(kH)^8}{2010^6} + \frac{(kH)^{10}}{1010^9}}$	0.11 %	0.11 %

Table 1: Phase velocity expressions and maximum of the relative error  $Er_C(s)$  compared with the Airy’s theory for different ranges of  $kH \in [0, s]$  for the non-linear hydrostatic shallow water system (SWE) and the Multilayer-HySEA (non-hydrostatic) system with  $j \geq 1$  layers (NH- $j$ L).

195 between the Airy’s theory and the systems (SWE) and (NH-1L). It is well known  
196 that waves generated by landslides, might present high characteristic values for  
197  $kH$ . For the (SWE) system, it is well known that it has an accurate phase  
198 velocity in a small range of  $kH$ , and that this system is appropriate for long  
199 waves as tsunami waves, but not for dispersive waves with higher values of  $kH$ .  
200 In the same vein, the one layer non-hydrostatic pressure system (NH-1L) can  
201 improve these results, but again, poor linear dispersive results are achieved in

202 a range of  $kH$  between 5 and 15. However, when the number of layers,  $L$ , is set  
 203 to 3 (still a small value) the system (1) is in an excellent agreement with the  
 204 Airy theory for  $kH$  up to 15. For the phase celerity, the percentage error is less  
 205 than 0.62%, and for the group velocity is less than 1% for  $kH$  smaller than 10  
 206 (see Figure 2). Linear shoaling is also well reproduced in this same range.

207 The Multilayer-HySEA model presents enhanced dispersive properties. In  
 208 order to have similar dispersive results as the ones obtained here using a three-  
 209 layer system, at least five layers are required for other similar multilayer models  
 210 as the one presented in Bai and Cheung (2018). Furthermore, the results pre-  
 211 sented for the phase velocity with two layers in Table 1 show that the system  
 212 proposed here produces smaller relative error for  $kH$  up to 15 compared with the  
 213 two-layer system in Cui et al. (2014). That means that the Multilayer-HySEA  
 214 model can achieve better dispersive properties than models having similar or  
 215 even more computational complexity.

### 216 *3.2. Modeling of breaking waves and wetting and drying treatment*

#### 217 *3.2.1. Modeling of breaking waves*

218 In shallow areas the breaking of waves can be observed near the coast. As  
 219 pointed out in Escalante et al. (2018a,b, 2019); Roeber et al. (2010) among  
 220 others, non-hydrostatic PDE systems such as the one considered in this paper  
 221 cannot describe this process without the inclusion of an additional term that  
 222 accounts for the dissipation of the amount of energy required when breaking  
 223 phenomena occur. In this work, we have implemented a simplified generalization  
 224 of the breaking mechanism that was introduced in Escalante et al. (2018a) for  
 225 the case of two layers. To do so, the vertical component of the stress-tensor is  
 226 depth-averaged on the vertical variable. Thus, adding the proposed integrated  
 227 viscosity term to system (1), only the vertical momentum equation changes and  
 228 reads for each  $\alpha \in \{1, 2, \dots, L\}$  as:

$$\partial_t (hw_\alpha) + \partial_x (hu_\alpha w_\alpha) + w_{\alpha+1/2}\Gamma_{\alpha+1/2} - w_{\alpha-1/2}\Gamma_{\alpha-1/2} = -h\partial_z p_\alpha + 2\zeta w_\alpha, \quad (9)$$

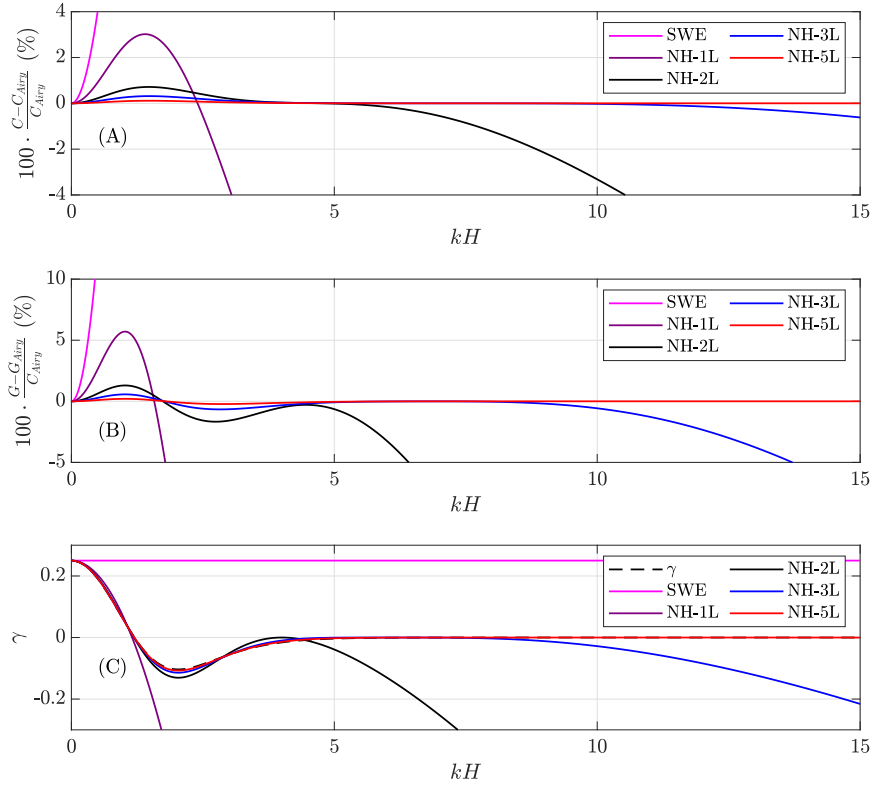


Figure 2: Relative error for the phase velocities (A), the group velocities (B), and comparison with the reference shoaling gradient (C), with respect to the Airy theory for the described multilayer systems (2L, 3L, and 5L), the one-layer non-hydrostatic, and the shallow-water system.

229 where  $\varsigma = \int_{z_{\alpha-1/2}}^{z_{\alpha-1/2}} \partial_z \nu$  is the eddy viscosity. In this work, as in Escalante et al.  
 230 (2018a); Roeber et al. (2010) we choose  $\varsigma$  to be

$$\varsigma = -KBh |\partial_x(h\bar{u})|, \quad (10)$$

231 where  $B$  is an empirical parameter related to a breaking criteria to switch on  
 232 and off this extra dissipation term. The definition of this empirical parameter  
 233 is based on a quasi-heuristic strategy to determine when the breaking occurs  
 234 (see Escalante et al. (2018b); Roeber et al. (2010) and references therein).

235 Finally, a natural and simple extension of the criterion proposed by Roeber

236 et al. (2010) is adopted

$$B = \max\left(1 - \frac{\partial_x(h\bar{u})}{U_1}, 0\right) \quad \text{for} \quad |\partial_x(h\bar{u})| \geq U_2, \quad (11)$$

237 where

$$U_1 = B_1\sqrt{gh}, \quad U_2 = B_2\sqrt{gh} \quad (12)$$

238 denote the flow speed at the onset and termination of the wave-breaking process  
 239 and  $B_1$ ,  $B_2$  are calibration coefficients. In this work, we use  $B_1 = 0.6$  and  
 240  $B_2 = 0.15$  for all the test cases studied. Finally, depending on the benchmark  
 241 problem, we use  $K \in \{2, 10\}$ .

### 242 3.2.2. Wetting and drying treatment

243 For the computation of variables in areas of small water depth, a wet-dry  
 244 treatment adapting the ideas described in Castro et al. (2005) is applied. The  
 245 key elements for the numerical treatment of wet-dry fronts with emerging bot-  
 246 tom topographies are based on:

- 247 • The hydrostatic pressure terms  $\partial_x\left(\frac{1}{2}gh^2\right) - gh\partial_x H = gh\partial_x\eta$  at the hori-  
 248 zontal velocity equations are modified for emerging bottoms to avoid spu-  
 249 rious pressure forces (see Castro et al. (2005)).
- 250 • To overcome the difficulties due to large round-off errors in computing  
 251 the velocities  $u_\alpha, w_\alpha$  from discharges for small values of  $h$ , we define the  
 252 velocities analogously as in Kurganov and Petrova (2007) applying the  
 253 desingularization formula

$$u_\alpha = \frac{\sqrt{2}hh u_\alpha}{\sqrt{h^4 + \max(h^4, \epsilon^4)}}, \quad w_\alpha = \frac{\sqrt{2}hh w_\alpha}{\sqrt{h^4 + \max(h^4, \epsilon^4)}}, \quad \alpha \in \{1, 2, \dots, L\} \quad (13)$$

254 which gives the exact value of  $u_\alpha$  and  $w_\alpha$  for  $h \geq \epsilon$ , and gives a smooth  
 255 transition of  $u_\alpha$  and  $w_\alpha$  to zero when  $h$  tends to zero without truncation.  
 256 In this work we set  $\epsilon = 10^{-3}$  for the numerical tests. A more detailed  
 257 discussion about the desingularization formula can be seen in Kurganov  
 258 and Petrova (2007).

259 **4. Numerical Solution Method**

260 We describe now the discretization of system (1) that follows the natural ex-  
 261 tension of the procedure described in Escalante et al. (2018a,b) for the one and  
 262 two layer non-hydrostatic system. The numerical scheme employed is based on  
 263 a two-step projection-correction method, similar to the standard Chorin’s pro-  
 264 jection method for Navier-Stokes equations (Chorin (1968)). This is a standard  
 265 procedure when dealing with dispersive systems (see Escalante et al. (2018b,a);  
 266 Ma et al. (2012); Kazolea and Delis (2013); Ricchiuto and Filippini (2014) and  
 267 references therein).

268 First, we shall solve the non-conservative hyperbolic underlying system (1)  
 269 given by the compact equation

$$\partial_t \mathbf{U} + \partial_x \mathbf{F}_{SW}(\mathbf{U}) + \mathbf{B}_{SW}(\mathbf{U}) \partial_x \mathbf{U} = \mathbf{G}_{SW}(\mathbf{U}) \partial_x H, \quad (14)$$

270 where the following compact notation has been used:

$$\mathbf{U} = \begin{pmatrix} h \\ hu_1 \\ \vdots \\ hu_L \\ hw_1 \\ \vdots \\ hw_L \end{pmatrix}, \quad \mathbf{F}_{SW}(\mathbf{U}) = \begin{pmatrix} hu \\ \frac{hu_1^2}{h} + \frac{1}{2}gh^2 \\ \vdots \\ \frac{hu_L^2}{h} + \frac{1}{2}gh^2 \\ hu_1w_1 \\ \vdots \\ hu_Lw_L \end{pmatrix}, \quad \mathbf{G}_{SW}(\mathbf{U}) = \begin{pmatrix} 0 \\ gh \\ \vdots \\ gh \\ 0 \\ \vdots \\ 0 \end{pmatrix}, \quad (15)$$

271 and  $\mathbf{B}_{SW}$  is a matrix such  $\mathbf{B}_{SW} \partial_x \mathbf{U}$  contains the non-conservative products  
 272 related to the mass transfer across interfaces appearing at the momentum equa-  
 273 tions.

274 Then, in a second step, non-hydrostatic terms given by the pressure vector

275 correction term

$$\mathcal{T}_{\mathcal{NH}}(h, \partial_x h, H, \partial_x H, \mathbf{P}, \partial_x \mathbf{P}) = - \begin{pmatrix} 0 \\ h(\partial_x p_1 + \sigma_1 \partial_z p_1) \\ \vdots \\ h(\partial_x p_L + \sigma_L \partial_z p_L) \\ h \partial_z p_1 \\ \vdots \\ h \partial_z p_L \end{pmatrix}, \quad \mathbf{P} = \begin{pmatrix} p_1 \\ p_2 \\ \vdots \\ p_L \end{pmatrix}, \quad (16)$$

276 as well as the divergence constraints at each layer

$$\mathcal{B}(\mathbf{U}, \partial_x \mathbf{U}, H, \partial_x H) = \begin{pmatrix} \partial_x u_{1/2} + \sigma_{1/2} \partial_z u_{1/2} + \partial_z w_{1/2} \\ \vdots \\ \partial_x u_{L-1/2} + \sigma_{L-1/2} \partial_z u_{L-1/2} + \partial_z w_{L-1/2} \end{pmatrix}, \quad (17)$$

277 will be taken into account.

278 System (14) is discretized using a second order finite volume PVM positive-  
 279 preserving well-balanced path-conservative method (Castro and Fernández-Nieto,  
 280 2012). As usual, we consider a set of  $N$  finite volume cells  $I_i = [x_{i-1/2}, x_{i+1/2}]$   
 281 with constant lengths  $\Delta x$  and define

$$\mathbf{U}_i(t) = \frac{1}{\Delta x} \int_{I_i} \mathbf{U}(x, t) dx, \quad (18)$$

282 the cell average of the function  $\mathbf{U}(x, t)$  on cell  $I_i$  at time  $t$ . Concerning non-  
 283 hydrostatic terms, we consider mid-points  $x_i$  of each cell  $I_i$  and denote the  
 284 point values of the function  $\mathbf{P}$  at time  $t$  by

$$\mathbf{P}_i(t) = \begin{pmatrix} p_1(x_i, t) \\ p_2(x_i, t) \\ \vdots \\ p_L(x_i, t) \end{pmatrix} \quad (19)$$

285 Non-hydrostatic terms will be approximated by second order compact finite-  
 286 differences.

Let us detail the time stepping procedure followed. Assume given time steps  $\Delta t^n$ , and denote  $t^n = \sum_{k \leq n} \Delta t^k$ . To obtain second order accuracy in time, the two-stage second-order TVD Runge-Kutta scheme is adopted. At the  $k$ th stage,  $k \in \{1, 2\}$ , the two-step projection-correction method is given by

$$\left\{ \begin{array}{l} \frac{\mathbf{U}^{(\tilde{k})} - \mathbf{U}^{(k-1)}}{\Delta t} + \partial_x \mathbf{F}(\mathbf{U}^{(k-1)}) + \mathbf{B}(\mathbf{U}^{(k-1)}) \partial_x \mathbf{U}^{(k-1)} \\ \qquad \qquad \qquad = \mathbf{G}(\mathbf{U}^{(k-1)}) \partial_x H, \\ \frac{\mathbf{U}^{(k)} - \mathbf{U}^{(\tilde{k})}}{\Delta t} = \mathcal{T}(h^{(k)}, \partial_x h^{(k)}, H, \partial_x H, \mathbf{P}^{(k)}, \partial_x \mathbf{P}^{(k)}) \\ \mathcal{B}(\mathbf{U}^{(k)}, \partial_x \mathbf{U}^{(k)}, H, \partial_x H) = \mathbf{0} \end{array} \right. \quad \begin{array}{l} (20a) \\ (20b) \\ (20c) \end{array}$$

287 where  $\mathbf{U}^{(0)}$  is  $\mathbf{U}$  at the time level  $t^n$ ,  $\mathbf{U}^{(\tilde{k})}$  is an intermediate value in the two-  
 288 step projection-correction method that contains the numerical solution of the  
 289 hyperbolic system (14) at the corresponding  $k$ th stage of the Runge-Kutta, and  
 290  $\mathbf{U}^{(k)}$  is the  $k$ th stage estimate. After that, a final value of the solution at the  
 291  $t^{n+1}$  time level is obtained:

$$\mathbf{U}^{n+1} = \frac{1}{2} \mathbf{U}^n + \frac{1}{2} \mathbf{U}^{(2)}. \quad (21)$$

292 Observe that, equations (20b-20c) requires, at each stage of the calculation  
 293 respectively, to solve a Poisson-like equation for each one of the variables con-  
 294 tained in  $\mathbf{P}^{(k)}$ . The resulting linear system is solved using an iterative Jacobi  
 295 method combined with a scheduled relaxation (see Adsuaara et al. (2016); Es-  
 296 calante et al. (2018a,b)). Note that the usual CFL restriction must be imposed  
 297 for the computation of the time step  $\Delta t$ .

298 With respect to the breaking mechanism introduced in Subsection 3.2, these  
 299 terms are semi-implicitly discretized at the end of the second step of the pro-  
 300 posed numerical scheme, at each Runge-Kutta stage. The resulting numerical  
 301 scheme is well-balanced for the water at rest solution and is linearly  $L^\infty$ -stable  
 302 under the usual CFL condition related to the hydrostatic system. It is also  
 303 worth mentioning that the numerical scheme is positive preserving and can deal  
 304 with emerging topographies. Finally, its extension to 2D is straightforward. In

305 this case, the computational domain is decomposed into subsets with a simple  
306 geometry, called cells or finite volumes. The numerical algorithm is well suited  
307 for its implementation in GPU architectures, as is shown in Castro et al. (2011).  
308 Furthermore, the compactness of the numerical stencil and the natural and the  
309 massively parallelization of the Jacobi method makes it possible that the second  
310 step can also be implemented in GPUs (see Escalante et al. (2018b,a)). That re-  
311 sults in a high efficiency of the numerical code and much shorter computational  
312 times.

## 313 5. Benchmark Problem Comparisons

314 In this Section, the numerical results obtained with the Multilayer-HySEA  
315 model and the comparison with the measured lab data for waves generated by  
316 the movement of a rigid bottom surface or of a solid block are presented. In  
317 particular, BP1 deals with a 2D submarine solid slide, BP2 with a 3D subma-  
318 rine slide and, finally, BP3 consists of two 3D slides, one partially submerged  
319 and a second one representing a completely submarine slide. In all these cases,  
320 a moving bottom condition has been used to model the solid block movement.  
321 Regarding the wave breaking model, the breaking mechanism described in Sub-  
322 section 3.2 was implemented, adopting  $B_1 = 0.6$ ,  $B_2 = 0.15$  for all the bench-  
323 mark problems, and  $K = 10$  for the third benchmark and  $K = 2$  for the rest.  
324 The description of all these benchmarks can be found at LTMBW (2017) and  
325 Kirby et al. (2018).

### 326 5.1. Benchmark Problem 1: Two-dimensional submarine solid block

327 This benchmark problem is based on the 2D laboratory experiments of Grilli  
328 and Watts (2005) which were performed at the University of Rhode Island.  
329 Refer to the above-mentioned work to get a detailed description of the present  
330 benchmark. Figure 3 depicts the sketch of the laboratory experiment design.  
331 The 2D slide model is semi-elliptical, lead-loaded, and rolling down a smooth  
332 slope with a slope angle  $\theta = 15^\circ$  (2 mm above the slope), in between two vertical



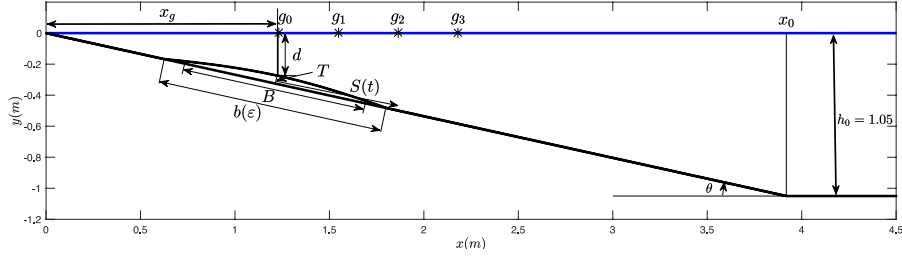


Figure 3: BP1. Sketch of main parameters and variables for wave generation by 2D rigid slide. [Modified from Grilli and Watts, 2005].

333 side walls, 20 cm apart. The water depth is  $h_0 = 1.05$  m over the flat bottom  
 334 part. The slide dimensions were, length  $B = 1$  m, maximum thickness  $T = T_{\text{ref}}$   
 335  $= 0.052$  m, and width  $w = 0.2$  m. The model initial submergence  $d$  was varied  
 336 in experiments and the free surface elevation recorded at 4 capacitance wave  
 337 gauges installed at locations:  $x' = 1.175, 1.475, 1.775,$  and  $2.075$  m, the first  
 338 location being nearly identical to  $x'_g = 1.168$  m (where de tilde variables, as  $x'$ ,  
 mean than non-dimensional units are used -see Table 3-).

$x'_g$	$T'$	$d'$	$\theta$	$B$	$b(\epsilon)$
1.168	0.052	0.259	15	1	1.225

Table 2: Values for variables defining setup configuration.

	$g_0$	$g_1$	$g_2$	$g_3$
$x$	1.234	1.549	1.864	2.179
$x' = x/h_0$	1.175	1.475	1.775	2.075

Table 3: Gauge positions in dimensional and non-dimensional units.

339

340 In this benchmark, two items remained not completely determined in the  
 341 original description provided: the first one is related with the initialization of  
 342 the numerical experiment, the second one is related with how and where the  
 343 solid moving block must stop. Other small issues related to the description of  
 344 the benchmark were put forward in Macías et al. (2017) at our NTHMP report.

345 The motion of the rigid slide was prescribed as a function of time as

$$S(t) = S_0 \log(\cosh(t/t_0)), \quad (22)$$

346 where  $S_0 = u_t^2/a_0 = 2.110 \text{ m}$ ,  $t_0 = u_t/a_0 = 1.677 \text{ s}$ ,  $a_0 = 0.75 \text{ m/s}^2$  and  $u_t =$   
 347  $1.258 \text{ m/s}$  is the terminal velocity. Figure 4 shows the prescribed acceleration,  
 348 velocity and rigid slide displacement. In the laboratory experiment, the block  
 349 is stopped at time  $t = t_0 = 1.667 \text{ s}$ . and we replicate this behaviour in the  
 350 numerical model. We also performed numerical experiments (not presented  
 351 here) where the block continued moving at constant speed.

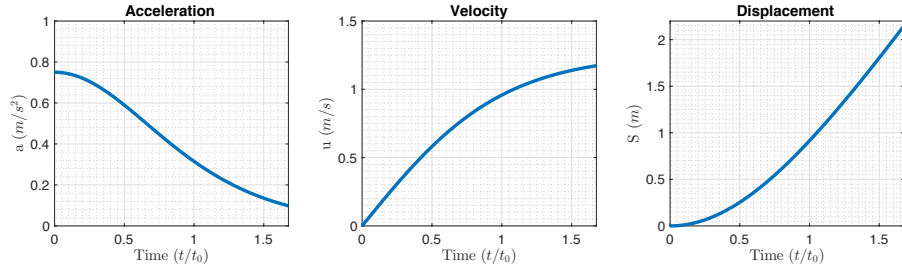


Figure 4: BP1. Prescribed acceleration, velocity and displacement of the solid slide.

352 The benchmark here consists of using the above information on slide shape,  
 353 submergence, and kinematics, together with reproducing the experimental set-  
 354 up to simulate surface elevations measured at the four wave gauges (average of  
 355 2 replicates of experiments provided).

356 Then, in order to reproduce the lab experiment, the interval  $[-1, 10]$  dis-  
 357 cretized with  $\Delta x = 0.02 \text{ m}$ , is the computational domain considered. In the  
 358 vertical, taking three layers seems to produce optimal results. Increasing the  
 359 number of layers gives similar results increasing the computational cost. The  
 360 stability  $CFL$  number was set to 0.9 and  $g = 9.81$ . The numerical simulation  
 361 performed was 4 s long in real time. As boundary conditions, outflow conditions  
 362 were imposed at  $x = -1$ ,  $x = 10$ .

363 In Figure 5 the comparison of the numerical results with the filtered lab  
 364 measured data is presented. A good overall agreement between them can be  
 365 observed. Some discrepancies can be seen after draw-down in all the gauges.

366 This behavior could also be observed, except for the last gauge, at Grilli and  
 367 Watts (2005) results. These authors explained that this behavior could be due  
 368 to unwanted surface tension effects. Given this comparison, and considering  
 369 the experimental variations and errors inherent to laboratory work and data  
 370 processing, it can be concluded that the Multilayer-HySEA model performs  
 371 optimally the present benchmark test.

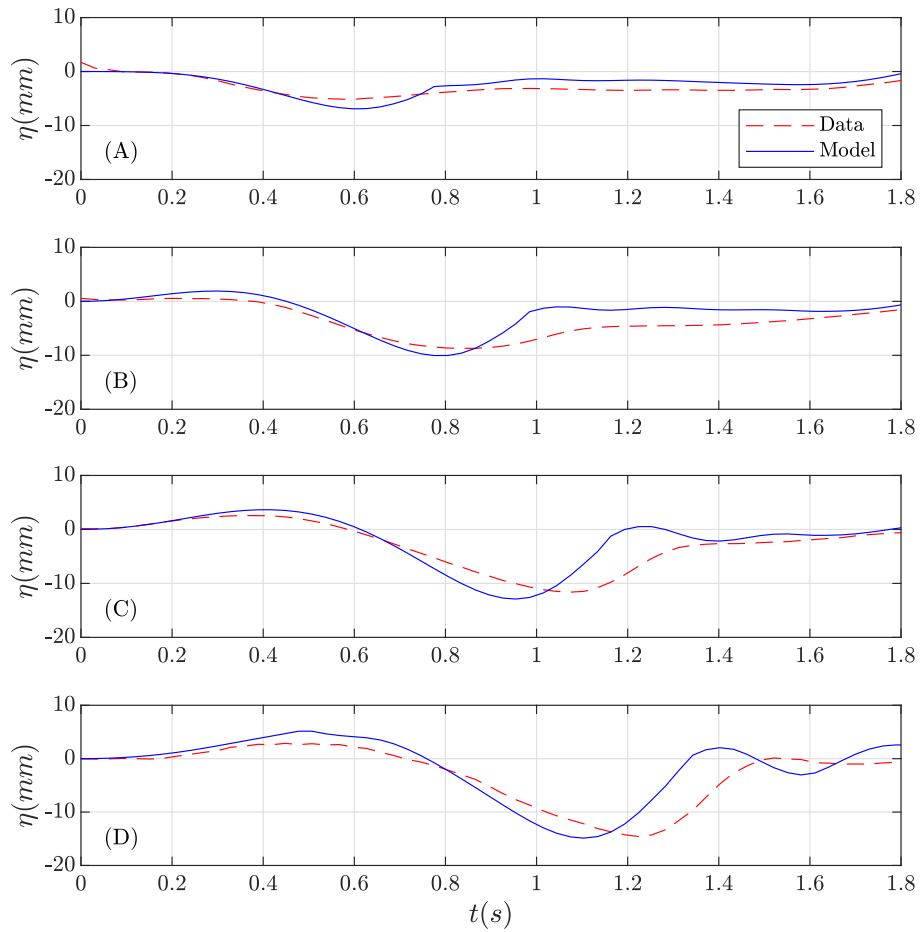


Figure 5: BP1. Filtered data (in red) and numerically simulated (in blue) time series at wave gauges (A)  $g_0$ , (B)  $g_1$ , (C)  $g_2$ , and (D)  $g_3$ .

372 5.2. Benchmark Problem 2: Three-dimensional submarine solid block

373 This second benchmark consists of a 3D extension of BP1. The longitudinal  
 374 sketch of the experiment is the same as in Figure 3. In the horizontal plane,  
 375 cross-sections are elliptic, the plan view of the rigid slide, for the case  $d = 61 \text{ mm}$ ,  
 376 is presented in Figure 6. It is based on the 3D laboratory experiments of Enet  
 377 and Grilli (2007). The experiments were also performed at the University of  
 378 Rhode Island in a water wave tank of width 3.6 m and length 30 m, with a still  
 379 water depth of 1.5 m over the flat bottom portion. As in the previous benchmark,  
 380 the angle of the plane slope where the slide slid down is  $\theta = 15^\circ$ . The submarine  
 381 slide model was built as a streamline Gaussian-shaped aluminum body with  
 382 elliptical footprint (see Figure 6), with down-slope length  $b = 0.395 \text{ m}$ , cross-  
 383 slope width  $w = 0.680 \text{ m}$ , and maximum thickness  $T = 0.082 \text{ m}$ . Complete  
 384 details about the analytic definition of the slide shape and the experimental  
 385 setting can be found at Kirby et al. (2018) and at LTMBW (2017).

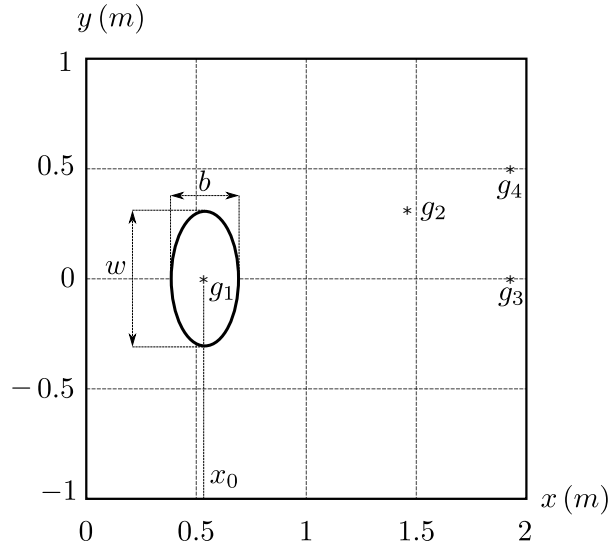


Figure 6: BP2. Sketch of the plan view (case 61 mm). [From Kirby et al. (2018)].

386 For the numerical simulations, the two-dimensional computational domain  
 387  $[-1, 10] \times [-1.8, 1.8]$  is considered and discretized with  $\Delta x = \Delta y = 0.02 \text{ m}$ . The  
 388 number of layers was set to 3. Numerical tests were performed using more layers

389 and similar results were obtained. The  $CFL$  number was set to 0.9 and  $g = 9.81$ .  
 390 The simulated time was 6 s. As boundary conditions, rigid wall conditions were  
 391 imposed at  $y = -1.8$ ,  $y = 1.8$  and outflow conditions at  $x = -1$ ,  $x = 10$ .

392 The benchmark test proposed consists in reproducing the slide shape and  
 393 complete experimental set-up in and using the information about submergence  
 394 and kinematics to replicate numerically Enet and Grilli's experiments for  $d =$   
 395 61 and  $d = 120$  mm. It is required to simulate surface elevations measured  
 396 at the four wave gauges (average of 2 replicates of experiments) and present  
 397 comparisons of the model with the experimental results.

398 Enet and Grilli (2007) performed experiments for 7 initial submergence  
 399 depths  $d$ . They are listed in Table 4, together with values of related slide  
 400 parameters and some measured tsunami wave characteristics. Here, the numer-  
 401 ical results corresponding to the two NTHMP required experiments (for  $d = 61$   
 402 and  $d = 120$  mm) will be presented first, then, as data for the seven experi-  
 403 ments were provided, the comparison for the remaining five cases will also be  
 404 presented.

$d$ (mm)	<b>61</b>	80	100	<b>120</b>	140	149	189
$x_g$ (mm) (measured)	551	617	696	763	846	877	1017
$x_g$ (mm) (theoretical)	560	630	705	780	854	888	1037
$\eta_0$ (mm)	13.0	9.2	7.8	5.1	4.4	4.2	3.1
$a_0$ (m/s)	1.20	1.21	1.19	1.17	1.14	1.20	1.21
$u_t$ (m/s)	1.70	1.64	1.93	2.03	2.13	1.94	1.97
$t_0$ (s)	1.42	1.36	1.62	1.74	1.87	1.62	1.63
$S_0$ (m)	2.408	2.223	3.130	3.522	3.980	3.136	3.207

Table 4: Measured and curve-fitted slide and wave parameters for the 7 experiments performed by Enet and Grilli (2007). Nomenclature: Measured characteristic amplitude  $\eta_0$  (at  $x = x_0$ ). Slide kinematics parameters  $a_0$ ,  $u_t$  and  $t_0$ .

405 In Figure 7 the comparison of the Multilayer-HySEA model numerical re-  
 406 sults with measured data for the first case,  $d = 61$  mm, in the four gauges, is

$g_1$	$g_2$	$g_3$	$g_4$
$(x_0,0)$	$(1469,350)$	$(1929,0)$	$(1929,500)$

Table 5: Wave gauge locations  $(x, y)$  in mm, as shown in Figure 6.

407 presented. An excellent agreement can be observed between these time series.  
408 The comparisons for the second required case ( $d = 120\text{ mm}$ ) in the 3 gauges  
409 with data provided (gauge  $g_3$  was not available) are shown in Figure 8. Good  
410 agreement can also be observed in this case. Finally, Figure 9 shows the com-  
411 parison for the five remaining cases provided by Enet and Grilli. In all cases (for  
412 all submergences), a good agreement between simulated results and measured  
413 lab data can be observed.

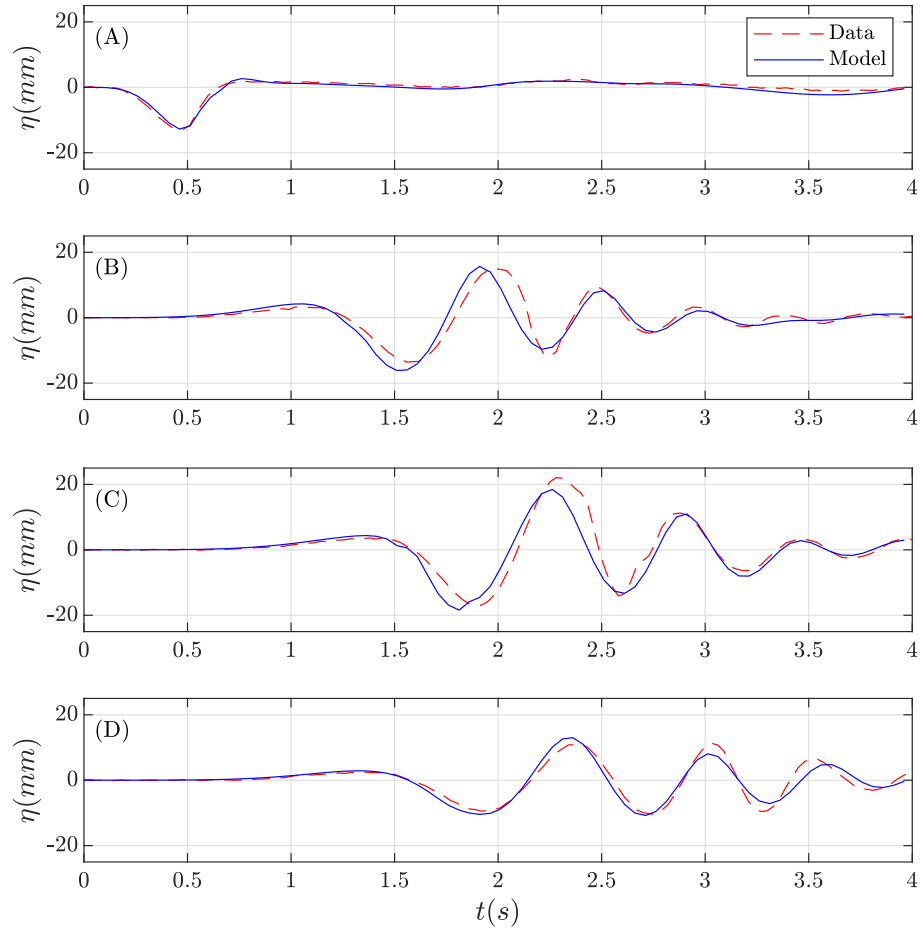


Figure 7: Test case  $d = 61$  mm. Numerically computed (in blue) time time series at wave gauges (A)  $g_1$ , (B)  $g_2$ , (C)  $g_3$ , and (D)  $g_4$  compared with the lab measured data (in red).

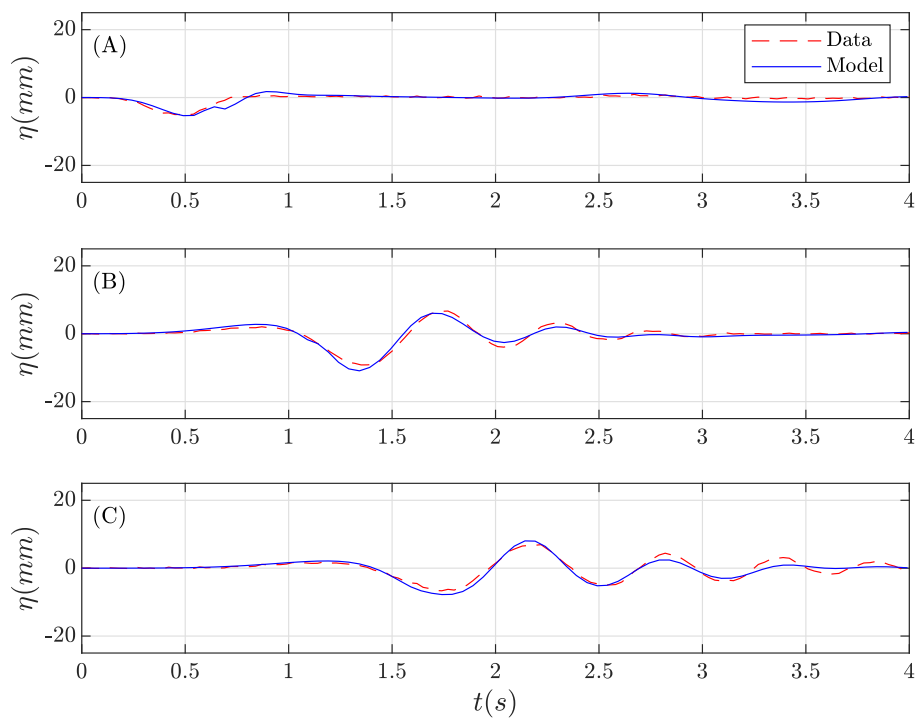


Figure 8: Test case  $d = 120$  mm. Numerically computed (in blue) time time series at wave gauges (A)  $g_1$ , (B)  $g_2$ , and (C)  $g_4$  for compared with the lab measured data (in red).



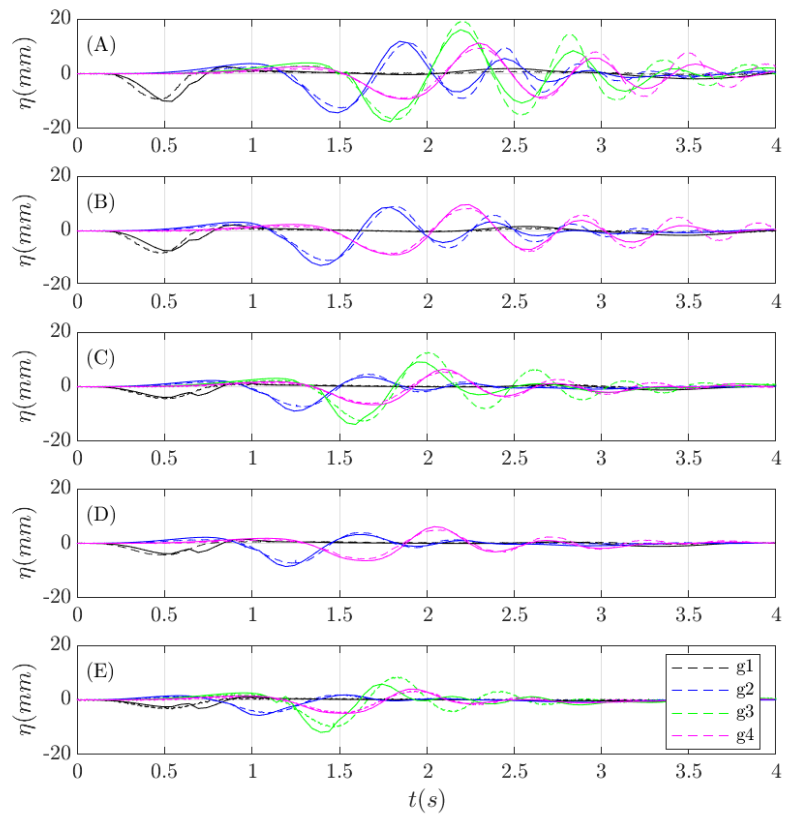


Figure 9: Comparison of data time series and numerical at wave gauges (dashed) for the cases (A)  $d = 80 \text{ mm}$ , (B)  $d = 100 \text{ mm}$ , (C)  $d = 140 \text{ mm}$ , (D)  $d = 149 \text{ mm}$ , and (E)  $d = 189 \text{ mm}$ .

414 In Table 6, the execution times for simulations performed on a NVIDIA Tesla  
 415 P100 GPU are presented. It can be observed that including non-hydrostatic  
 416 terms in the NLSW equations results in an increase of the computational time in  
 417 2.65 times. If a richer vertical structure is considered, then larger computational  
 418 times are required. As examples for the two and three-layer systems, 3.3 and  
 419 4.45 times increase in the computational effort.

	Runtime (s)	Ratio
SWE	23.08	1
1L-NH	61.20	2.65
2L-NH	76.35	3.30
3L-NH	102.93	4.45

Table 6: Execution times in seconds for SWE and non-hydrostatic GPU implementations. Ratios compared with SWE.

420 Figure 10 shows the comparison, for the four models considered, of the  
 421 numerical results obtained with the measured data at gauge  $g_4$  for the case  
 422  $d = 189 \text{ mm}$ . It can be observed that a model vertical structure considering  
 423 only one layer is not enough to reproduce the observed data, and that consid-  
 424 ering 2 and 3 layers in the model produce much better numerical results.

425 Moreover, Table 7 shows the period times,  $T$ , of the time series data in  
 426 Figures 7, 8, and 9 for all the wave gauges. To obtain the vales for the periods,  
 427 we have computed the elapsed time between the first two wave troughs in each  
 428 time series. We have omitted the measurement for wave gauge  $g_1$  because it  
 429 was not clear how to measure the period in this case. Once the period from  
 430 each time series has been measured, we have computed the wave number from  
 431 the dispersion relation given from the Airy theory:

$$\frac{2\pi}{T} = \sqrt{gk \tanh(kH)}. \quad (23)$$

432 Table 8 shows the computed values  $kH$  by solving the dispersion relation (23).  
 433 On the view of the computed  $kH$  values it can be stated that  $kH \in [2.815, 4.528]$ .  
 434 Since multilayer models have good dispersion relation errors within this range

435 of  $kH$  (see Table 1 and Figure 2), this explains the aforementioned excellent  
 436 agreement between the computed time series and the measured lab data.  
 437 Finally, although the phase velocity for the one-layer system shows an error  
 438 bounded by only 3.02% for  $kH \in [0, 5]$  (see Table 1), it can be seen in Figure 10  
 439 that the one-layer non-hydrostatic pressure system cannot represent the waves  
 440 correctly. In contrast, the one-layer system tends to amplify waves. This be-  
 441 haviour can be explained by observing the shoaling gradient for this model (see  
 442 Figure 2). The shoaling gradient verifies the ODE

$$A' = -A \cdot \gamma(kH) \cdot \frac{\partial_x H}{H}, \quad (24)$$

443 where  $A$  denotes the amplitude. Then, it can be stated by inspecting the so-  
 444 lutions of the ODE (24) that if the shoaling gradient of the model  $\gamma(kH)$  is  
 445 underestimated with respect to the Airy theory ( $\gamma < \gamma_{Airy}$ ), then the solutions  
 446 of the system tend to amplify waves, in this case, for offshore wave propagation.  
 447 The poor behavior shown by the one-layer system in some cases justifies the  
 need to incorporate the improved multilayer model considered here.

$d$ (mm)	61	80	100	120	140	149	189
$g_2$	0.69	0.686	0.704	0.69	0.676	0.692	0.8
$g_3$	0.66	0.716	–	–	0.702	–	0.694
$g_4$	0.84	0.8	0.784	0.75	0.794	0.784	0.751

Table 7: Measured wave period  $T$  (s) for test cases  $d = 61, 120$  (Figures 7 and 8) and  
 $d = 80, 100, 140, 149, 189$  (Figure 9).

448

### 449 5.3. Benchmark Problem 3: Three-dimensional submarine/subaerial triangular 450 solid block

451 This benchmark problem is based on the 3D laboratory experiment of Wu  
 452 (2004) and Liu et al. (2005), for a series of triangular blocks of several aspect  
 453 ratios moving down a plane slope into the water from a dry (subaerial) or wet  
 454 (submarine) location. Figure 11 shows the schematic description of the set-up  
 455 for this benchmark in the case of a partially submerged block. Further details

$d$ (mm)	61	80	100	120	140	149	189
$g_2$	3.114	3.15	2.995	3.114	3.242	3.097	2.35
$g_3$	4.528	3.85	–	–	4.004	–	4.097
$g_4$	2.815	3.093	3.218	3.512	3.14	3.218	3.512

Table 8: Computed  $kH$  values from the measured wave period (see Table 7) and the Airy dispersion relation  $2\pi/T = \sqrt{gk \tanh(kH)}$  for test cases  $d = 61, 80, 100, 120, 140, 149$  and  $189$ .

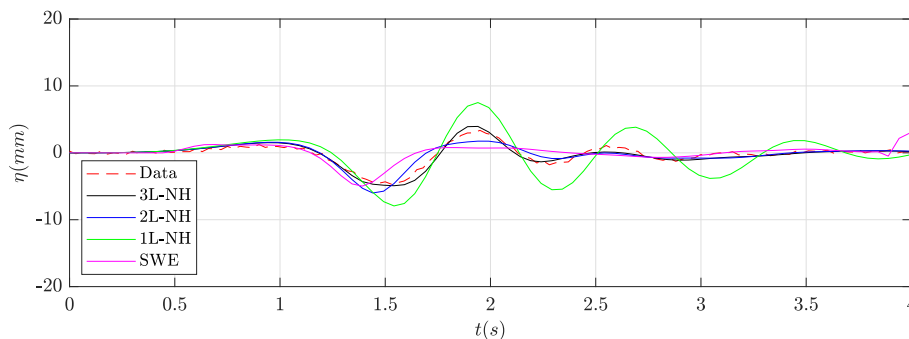


Figure 10: Test case  $d = 189$  mm. Lab measured data (red) and numerically computed time series at wave gauge  $g_4$  using different numerical models.

456 can be found at Kirby et al. (2018) and at LTMBW (2017). The laboratory  
 457 experiments were conducted in a wave tank at Oregon State University of length  
 458 104 m, width 3.7 m, and depth 4.6 m.

459 A plane slope 1:2 (as the one shown in Figure 11 upper panel) with  $\theta = 26.6^\circ$   
 460 was located near one end of the tank and a dissipating beach in the other. In all  
 461 the experiments, the water depth was  $h_0 = 2.44$  m. The experiments retained  
 462 for the present benchmark were all performed with a triangular block of length  
 463  $b = 0.91$  m, width  $w = 0.61$  m, and vertical front face  $a = b/2 = 0.455$  m.

464 The block movement was provided by means of a polynomial fitting to mea-  
 465 sured data, giving the horizontal distance as:

$$x_{0,t} = x_{(0,t=0)} + (at^3 + bt^2 + ct) \cos \beta, \quad (25)$$

466 with  $\beta = \arctan(1/2)$  and  $x_{(0,t=0)} = -2\Delta$ . The polynomial coefficients for the  
 467 two cases proposed are given in Table 9.

$\Delta$	$a$	$b$	$c$
0.10 m	-0.097588	0.759361	0.078776
-0.25 m	-0.085808	0.734798	-0.034346

Table 9: Polynomial coefficients defining slide motion.

468 For each case, measured free surface elevations for two wave gauges placed  
469 at  $(x, y) = (1.83, 0)$  (in m) and  $(x, y) = (1.2446, 0.635)$ , where  $x$  is the distance  
470 to the initial coastline and  $y$  is the distance to the central cross-section (see  
471 location at Fig. 11 lower panel). Also measured runup for each case is given at  
472 runup gauges 2 and 3 in Figure 11 lower panel, lying on the slope at a distance  
473 0.305 m and 0.611 m from the central cross-section, respectively.

474 The two-dimensional computational domain  $[-2, 6] \times [-2, 2]$  is discretised  
475 with  $\Delta x = \Delta y = 0.025$  m and the number of layers was set up to 3. Numerical  
476 experiments using more number of layers were performed, obtaining similar  
477 results. The stability CFL number was set to 0.9 and  $g = 9.81$ . The simulated  
478 time was 4 s. The same boundary conditions, as in the previous case, were  
479 imposed.

480 The numerical results obtained for the subaerial test case are presented in  
481 Figures 12 and 13. Figure 12 depicts the comparison for the time series at the  
482 wave gauges and Figure 13 at the runup gauges. The same comparison has been  
483 performed for the submerged test case, and it is presented in Figures 14 and  
484 15. The agreement for the wave gauges is quite good for WG1 in both cases.  
485 For WG2, just in front of the block, an overshoot after the first depression wave  
486 is observed in both cases related to the turbulent nature of the experiment.  
487 Note that although a turbulent model is not considered here, we have noted  
488 that the breaking criteria helps to dissipate energy associated to this turbulent  
489 process. For the run-up, the qualitative agreement is quite good, with the larger  
490 discrepancies in RG3 for the submarine test case.

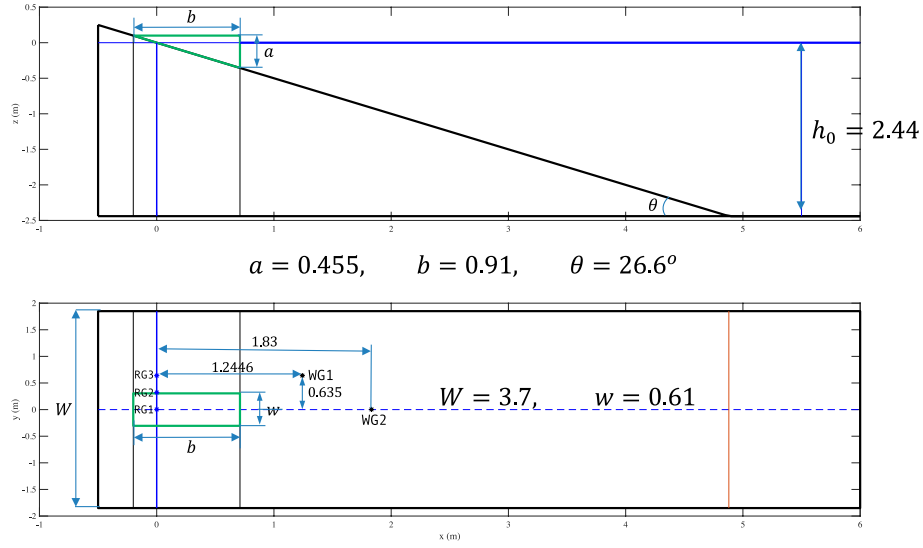


Figure 11: Definition sketch for BP3 laboratory experiments. Here for a submerged ( $\Delta < 0$ ) slide. Upper panel vertical cross section, lower panel plan view. All units are in meters.

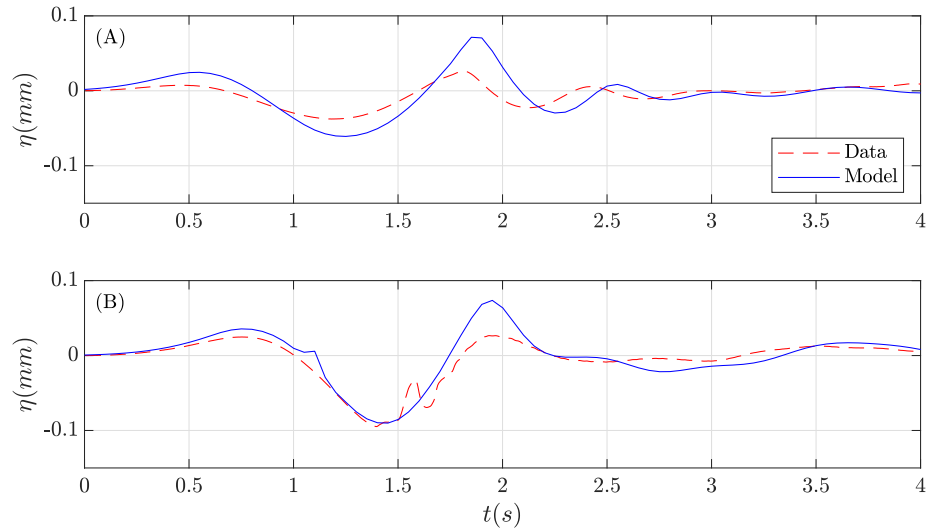


Figure 12: Subaerial test case. Lab measured water height (red) and numerical time series (blue) at wave gauges (A) WG1 and (B) WG2 .

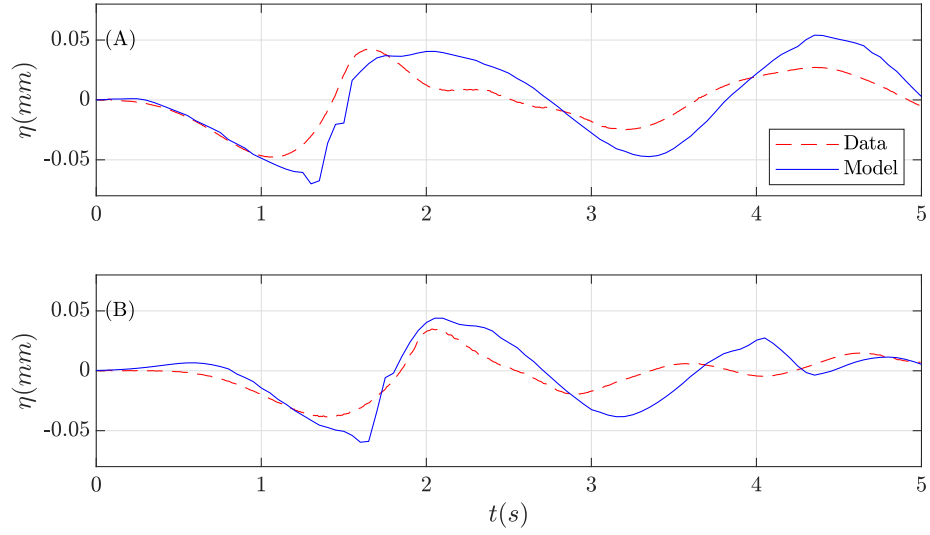


Figure 13: Subaerial test case. Lab measured runup (red) and numerical time series (blue) at runup gauges (A) RG2 and (B) RG3.

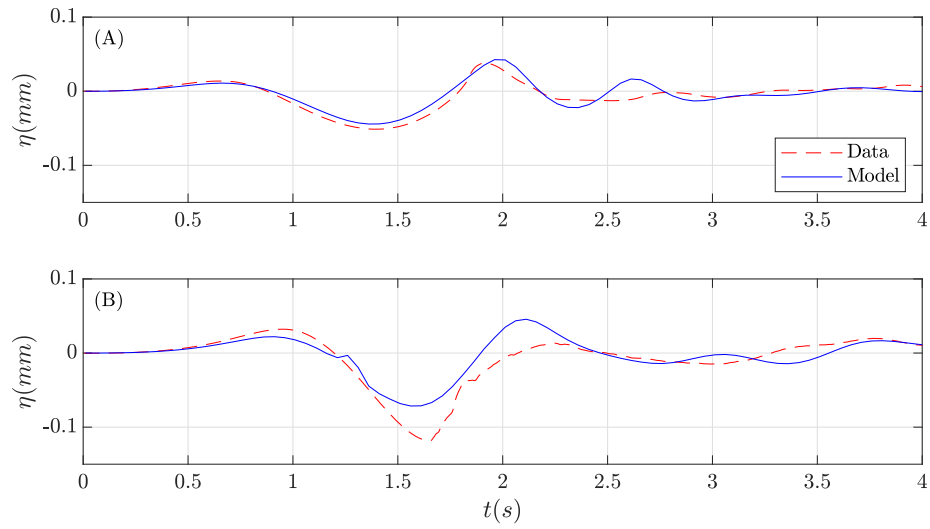


Figure 14: Submerged test case. Lab measured water height (red) and numerical time series (blue) at wave gauges (A) WG1 and (B) WG2.

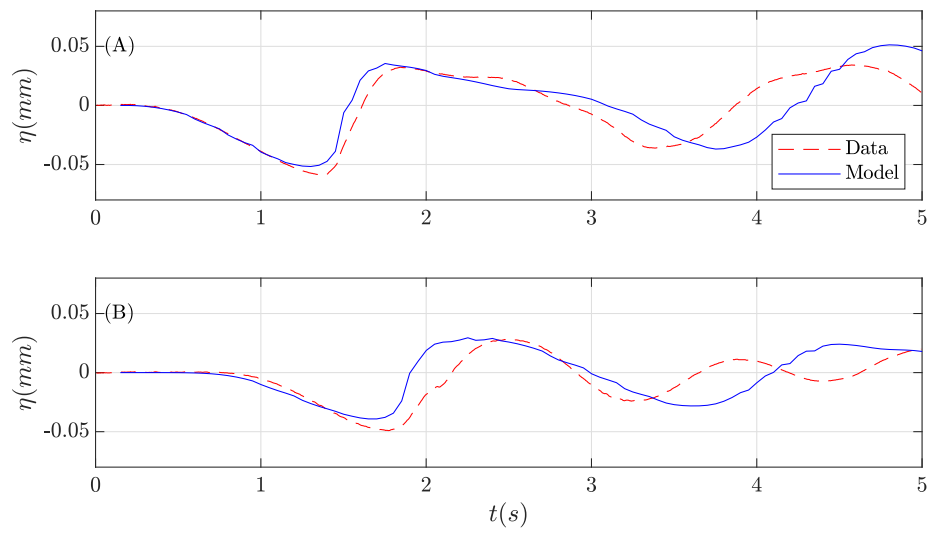


Figure 15: Submerged test case. Lab measured runup (red) and numerical time series (blue) at runup gauges (A) RG2 and (B) RG3.



## 491 **6. Concluding Remarks**

492 Validation of numerical models is a first unavoidable step before their use  
493 as predictive tools. This requirement is even more necessary when the devel-  
494 oped models are going to be used for risk assessment in natural events where  
495 human lives are involved. The present work is the first step in this task for the  
496 Multilayer-HySEA model, a novel dispersive multilayer model of the HySEA  
497 suite developed at the University of Malaga. This model considers a stratified  
498 vertical structure and includes non-hydrostatic terms, this is done in order to  
499 include the dispersive effects in the propagation of the waves in a homogeneous,  
500 inviscid, and incompressible fluid. The numerical scheme implemented, com-  
501 bines a highly robust and efficient finite volume path-conservative scheme for  
502 the underlying hyperbolic system and finite differences for the discretization of  
503 the non-hydrostatic terms. In order to increase numerical efficiency, the numeri-  
504 cal model is implemented to run in GPU architectures. In particular in NVIDIA  
505 graphics cards and using CUDA language. In the case of the traditional SW  
506 non-dispersive model, this kind of implementations produces an extremely ef-  
507 ficient and fast code (Macías et al., 2020d). Increasing the number of layers  
508 in SW models provides an enhanced vertical resolution and, at the same time,  
509 increases the computational cost. Despite this, from a computational point of  
510 view, the two-layer non-hydrostatic code presents a good computational effi-  
511 ciency, and computing times with respect to the one layer SWE GPU code are  
512 absolutely reasonable, being only from 2 to 2.5 larger than for the one layer case.  
513 In the numerical simulations performed in the present work, the non-hydrostatic  
514 wall-clock times are always below 4.45 times those for the traditional SWE Hy-  
515 SEA model, for a number of vertical layers up to three. The numerical scheme  
516 presented here and the corresponding multilayer SW water model proposed, is  
517 highly efficient and is able to model dispersive effects with a low computational  
518 cost.

519 Regarding model results, they show a good agreement with the experimental  
520 data for the three benchmark problems studied in the present work. In partic-

521 ular, for BP2, but this also occurs for the other two benchmark problems, we  
522 have shown that a one layer, hydrostatic or non-hydrostatic, model is not able  
523 to reproduce the complexity in the observed lab data considered in the pro-  
524 posed benchmarks. The waves to be modeled in the test cases proposed here  
525 are high-frequency and dispersive. Hence, it is at least necessary a two-layer  
526 structure and non-hydrostatic terms in the model to be used in order to capture  
527 the dynamics of the generated waves. As noted in Kirby et al. (2018) and in  
528 view of the results presented, the non-hydrostatic multilayer model discussed  
529 here can adequately represent the physics and behavior of the waves generated  
530 with a reasonable low computational cost.

## 531 **7. Code and data availability**

532 The numerical code used to perform the numerical simulations in this paper  
533 is available at HySEA codes web page at <https://edanya.uma.es/hysea/index.php/>  
534 download.

535 All the data used in the present work and necessary to reproduce the exper-  
536 iments set-up of the numerical experiments and the laboratory measured data  
537 to compared with, can be downloaded from LTMBW (2017) at the web site  
538 <http://www1.udel.edu/kirby/landslide/>. Finally, the NetCDF files containing  
539 the numerical results obtained with the Multilayer-HySEA code can be found  
540 and download from Macías et al. (2020b).

## 541 **8. Authors' contributions**

542 JM is leading the HySEA codes benchmarking effort undertaken by the  
543 EDANYA group, he wrote most of the paper, reviewed and edited it, assisted in  
544 the numerical experiments and in their set up. CE implemented the numerical  
545 code and performed all the numerical experiments, he also contributed to writing  
546 the manuscript. JM and CE did all the figures. MC strongly contributed to the  
547 design and implementation of the numerical code.

548 **9. Competing interest**

549 The authors declare that they have no conflict of interest.

550 **10. Acknowledgements**

551 This research has been partially supported by the Spanish Government-  
552 FEDER funded project MEGAFLOW (RTI2018-096064-B-C21), the Junta de  
553 Andalucía-FEDER funded project UMA18-Federja-161 and the University of  
554 Málaga, Campus de Excelencia Internacional Andalucía Tech.

555 **References**

- 556 Adsuara, J., Cordero-Carrión, I., Cerdá-Durán, P., Aloy, M., 2016. Scheduled  
557 relaxation Jacobi method: Improvements and applications. *Journal of Com-*  
558 *putational Physics* 321, 369–413.
- 559 de la Asunción, M., Castro, M., González-Vida, J., Macías, J., Ortega, S.,  
560 Sánchez-Linares, C., 2013. East Coast Non-Seismic Tsunamis: A first land-  
561 slide approach. Technical Report. NOAA report.
- 562 Ataie-Ashtiani, B., Najafi-Jilani, A., 2008. Laboratory investigations on impul-  
563 sive waves caused by underwater landslide. *Coastal Engineering* 55, 989 –  
564 1004. doi:10.1016/j.coastaleng.2008.03.003.
- 565 Bai, Y., Cheung, K.F., 2018. Linear shoaling of free-surface waves in multi-  
566 layer non-hydrostatic models. *Ocean Modelling* 121, 90 – 104. doi:10.1016/  
567 j.ocemod.2017.11.005.
- 568 ten Brink, U., Chaytor, J., Geist, E., Brothers, D., Andrews, B., 2014. Assess-  
569 ment of tsunami hazard to the U.S. Atlantic margin. *Marine Geology* 353, 31  
570 – 54. doi:10.1016/j.margeo.2014.02.011.
- 571 Castro, M., Fernández-Nieto, E., 2012. A class of computationally fast first order  
572 finite volume solvers: PVM methods. *SIAM Journal on Scientific Computing*  
573 34, A2173 – A2196. doi:10.1137/100795280.

- 574 Castro, M., Ferreiro, A., García, J., González, J., Macías, J., Parés, C., Vázquez-  
575 Cendón, M., 2005. The numerical treatment of wet/dry fronts in shallow  
576 flows: Applications to one-layer and two-layer systems. *Mathematical and*  
577 *Computer Modelling* 42, 419–439.
- 578 Castro, M., Ortega, S., de la Asunción, M., Mantas, J., Gallardo, J., 2011. GPU  
579 computing for shallow water flow simulation based on finite volume schemes.  
580 *Comptes Rendus Mécanique* 339, 165–184.
- 581 Chorin, A., 1968. Numerical solution of the navier-stokes equations. *Mathe-*  
582 *matics of Computation* 22, 745–762. URL: [http://www.jstor.org/stable/](http://www.jstor.org/stable/2004575)  
583 [2004575](http://www.jstor.org/stable/2004575).
- 584 Cui, H., Pietrzak, J., Stelling, G., 2014. Optimal dispersion with minimized  
585 Poisson equations for non-hydrostatic free surface flows. *Ocean Modelling*  
586 81, 1 – 12. doi:10.1016/j.ocemod.2014.06.004.
- 587 Enet, F., Grilli, S., 2007. Experimental study of tsunami generation by three-  
588 dimensional rigid underwater landslides. *Journal of Waterway, Port, Coastal,*  
589 *and Ocean Engineering* 133, 442–454. doi:10.1061/(ASCE)0733-950X(2007)  
590 133:6(442).
- 591 Escalante, C., Dumbser, M., Castro, M.J., 2019. An efficient hyperbolic re-  
592 laxation system for dispersive non-hydrostatic water waves and its solution  
593 with high order discontinuous Galerkin schemes. *Journal of Computational*  
594 *Physics* 394, 385–416. doi:10.1016/j.jcp.2019.05.035.
- 595 Escalante, C., Fernández-Nieto, E., Morales, T., Castro, M., 2018a. An efficient  
596 two-layer non-hydrostatic approach for dispersive water waves. *Journal of*  
597 *Scientific Computing* doi:10.1007/s10915-018-0849-9.
- 598 Escalante, C., Morales, T., Castro, M., 2018b. Non-hydrostatic pressure shallow  
599 flows: GPU implementation using finite volume and finite difference scheme.  
600 *Applied Mathematics and Computation* 338, 631 – 659. doi:10.1016/j.amc.  
601 2018.06.035.

- 602 Fernández, E., Bouchut, F., Bresh, D., Castro, M., Mangeney, A., 2008. A new  
603 Savage-Hutter type model for submarine avalanches and generated tsunami.  
604 *J. Comp. Phys.* 227, 7720–7754.
- 605 Fernández-Nieto, E., Parisot, M., Penel, Y., Sainte-Marie, J., 2018. A hierarchy  
606 of dispersive layer-averaged approximations of Euler equations for free surface  
607 flows. *Communications in Mathematical Sciences* 16, 1169–1202.
- 608 Fritz, D., Hager, W., Minor, H.E., 2001. Lituya Bay case: rockslide impact and  
609 wave runup. *Science of Tsunami Hazards* 19(1), 3–22.
- 610 González-Vida, J., Macías, J., Castro, M., Sánchez-Linares, C., Ortega-Acosta,  
611 S., Arcas, D., 2019. The Lituya Bay landslide-generated mega-tsunami. Nu-  
612 merical simulation and sensitivity analysis. *Nat. Hazards Earth Syst. Sci.* 19,  
613 369–388. doi:10.5194/nhess-19-369-2019.
- 614 Grilli, S., Vogelmann, S., Watts, P., 2002. Development of a 3D numerical  
615 wave tank for modeling tsunami generation by underwater landslides. *En-  
616 gineering Analysis with Boundary Elements* 26, 301 – 313. doi:10.1016/  
617 S0955-7997(01)00113-8.
- 618 Grilli, S., Watts, P., 1999. Modeling of waves generated by a moving submerged  
619 body. applications to underwater landslides. *Engineering Analysis with  
620 Boundary Elements* 23, 645 – 656. doi:10.1016/S0955-7997(99)00021-1.
- 621 Grilli, S., Watts, P., 2005. Tsunami generation by submarine mass failure.  
622 I: Modeling, experimental validation, and sensitivity analyses. *Journal of  
623 Waterway, Port, Coastal, and Ocean Engineering* 131, 283–297. doi:10.1061/  
624 (ASCE)0733-950X(2005)131:6(283).
- 625 Heller, V., Hager, W., 2011. Waves types of landslide generated impulse waves.  
626 *Ocean Engineering* 38, 630–640.
- 627 Horrillo, J., Grilli, S., Nicolisky, D., Roeber, V., Zhang, J., 2015. Per-  
628 formance benchmarking tsunami models for NTHMP’s inundation map-

629 ping activities. *Pure and Applied Geophysics* 172, 869–884. doi:10.1007/  
630 s00024-014-0891-y.

631 Iglesias, O., 2015. Generación y propagación de tsunamis en el  
632 mar Catalano-Balear. Ph.D. thesis. Universitat de Barcelona.  
633 [<http://hdl.handle.net/2445/68704>].

634 Kazolea, M., Delis, A.I., 2013. A well-balanced shock-capturing hybrid finite  
635 volume-finite difference numerical scheme for extended 1D Boussinesq models.  
636 *Applied Numerical Mathematics* 67, 167–186. doi:10.1016/j.apnum.2011.  
637 07.003.

638 Kirby, J., Grilli, S., Zhang, C., Horrillo, J., Nicolsky, D., Liu, P.L.F., 2018. The  
639 NTHMP Landslide Tsunami Benchmark Workshop, Galveston, January 9-11,  
640 2017. Technical Report. Research Report CACR-18-01.

641 Kurganov, A., Petrova, G., 2007. A second-order well-balanced positivity  
642 preserving central-upwind scheme for the saint-venant system. *Commun.*  
643 *Math. Sci.* 5, 133–160. URL: [https://projecteuclid.org/443/euclid.](https://projecteuclid.org/443/euclid.cms/1175797625)  
644 [cms/1175797625](https://projecteuclid.org/443/euclid.cms/1175797625).

645 Liu, P.L.F., Wu, T.R., Raichlen, F., Synolakis, C.E., Borrero, J.C., 2005. Runup  
646 and rundown generated by three-dimensional sliding masses. *Journal of Fluid*  
647 *Mechanics* 536, 107–144. doi:10.1017/S0022112005004799.

648 Liu, P.L.F., Yeh, H., Synolakis, C., 2008. *Advanced Numerical Models for Sim-*  
649 *ulating Tsunami Waves and Runup.* WORLD SCIENTIFIC. URL: [https:](https://www.worldscientific.com/doi/abs/10.1142/6226)  
650 [//www.worldscientific.com/doi/abs/10.1142/6226](https://www.worldscientific.com/doi/abs/10.1142/6226), doi:10.1142/6226,  
651 [arXiv:https://www.worldscientific.com/doi/pdf/10.1142/6226](https://www.worldscientific.com/doi/pdf/10.1142/6226).

652 LTMBW, 2017. Landslide Tsunami Model Benchmarking Workshop, Galve-  
653 ston, Texas, 2017. <http://www1.udel.edu/kirby/landslide/index.html>.  
654 Accessed: 2020-04-25.

655 Lynett, P., Gately, K., Wilson, R., Montoya, L., Arcas, D., Aytore, B., Bai,  
656 Y., Bricker, J., Castro, M., Cheung, K., David, C., Dogan, G., Escalante, C.,

- 657 González-Vida, J., Grilli, S., Heitmann, T., Horrillo, J., Kanouglu, U., Kian,  
658 R., Kirby, J., Li, W., Macías, J., Nicolsky, D., Ortega, S., Pampell-Manis, A.,  
659 Park, Y., Roeber, V., Sharghivand, N., Shelby, M., Shi, F., Tehranirad, B.,  
660 Tolkova, E., Thio, H., Velioglu, D., Yalciner, A., Yamazaki, Y., Zaytsev, A.,  
661 Zhang, Y., 2017. Inter-model analysis of tsunami-induced coastal currents.  
662 *Ocean Modelling* 114, 14 – 32. doi:10.1016/j.ocemod.2017.04.003.
- 663 Lynnett, P., Liu, P.L.F., 2002. A numerical study of subma-  
664 rine-landslide-generated waves and run-up. *Proceedings of the Royal So-*  
665 *ciety of London A: Mathematical, Physical and Engineering Sciences* 458,  
666 2885–2910. doi:10.1098/rspa.2002.0973.
- 667 Lynnett, P., Liu, P.L.F., 2004. A two-layer approach to wave modelling. *Pro-*  
668 *ceedings of the Royal Society of London A: Mathematical, Physical and En-*  
669 *gineering Sciences* 460, 2637–2669.
- 670 Ma, G., Shi, F., Kirby, J., 2012. Shock-capturing non-hydrostatic model for  
671 fully dispersive surface wave processes. *Ocean Modelling* 43–44, 22–35.
- 672 Macías, J., Castro, M., Ortega, S., Escalante, C., González-Vida, J., 2017.  
673 Performance benchmarking of Tsunami-HySEA model for NTHMP’s in-  
674 undation mapping activities. *Pure and Applied Geophysics* doi:10.1007/  
675 s00024-017-1583-1.
- 676 Macías, J., Escalante, C., Castro, M., 2020a. Multilayer-HySEA model valida-  
677 tion for landslide generated tsunamis. Part II Granular slides. *Nat. Hazards*  
678 *Earth Syst. Sci. Discuss.* doi:10.5194/nhess-2020-172.
- 679 Macías, J., Escalante, C., Castro, M., 2020b. Numerical results in Multilayer-  
680 HySEA model validation for landslide generated tsunamis. Part I Rigid slides.  
681 Dataset on Mendeley. Doi: 10.17632/xtfzrbvcb2.3.
- 682 Macías, J., Escalante, C., Castro, M., 2020c. Performance assessment of  
683 Tsunami-HySEA model for NTHMP tsunami currents benchmarking. lab-

684 oratory data. *Coastal Engineering* 158. doi:10.1016/j.coastaleng.2020.  
685 103667.

686 Macías, J., Escalante, C., Castro, M., González-Vida, J., Ortega, S., 2017. Hy-  
687 SEA model. Landslide Benchmarking Results. Technical Report. In NTHMP  
688 report. doi:10.13140/RG.2.2.27081.60002.

689 Macías, J., Ortega, S., González-Vida, J., Castro, M., 2020d. Performance  
690 assessment of Tsunami-HySEA model for NTHMP tsunami currents bench-  
691 marking. field cases. *Ocean Modeling* 152, 101645. doi:https://doi.org/  
692 10.1016/j.ocemod.2020.101645.

693 Macías, J., Vázquez, J., Fernández-Salas, L., González-Vida, J., Bárcenas, P.,  
694 Castro, M., del Río, V.D., Alonso, B., 2015. The Al-Borani submarine land-  
695 slide and associated tsunami. A modelling approach. *Marine Geology* 361, 79  
696 – 95. doi:10.1016/j.margeo.2014.12.006.

697 Madsen, P., Sorensen, O., 1992. A new form of the Boussinesq equations  
698 with improved linear dispersion characteristics. Part 2: A slowly varying  
699 bathymetry. *Coastal Engineering* 18, 183–204.

700 Ricchiuto, M., Filippini, A.G., 2014. Upwind residual discretization of enhanced  
701 Boussinesq equations for wave propagation over complex bathymetries. *Jour-  
702 nal of Computational Physics* 271, 306–341. URL: [http://dx.doi.org/10.](http://dx.doi.org/10.1016/j.jcp.2013.12.048)  
703 [1016/j.jcp.2013.12.048](http://dx.doi.org/10.1016/j.jcp.2013.12.048), doi:10.1016/j.jcp.2013.12.048.

704 Roeber, V., Cheung, K.F., Kobayashi, M.H., 2010. Shock-capturing Boussinesq-  
705 type model for nearshore wave processes. *Coastal Engineering* 57, 407–423.  
706 URL: <http://dx.doi.org/10.1016/j.coastaleng.2009.11.007>, doi:10.  
707 [1016/j.coastaleng.2009.11.007](http://dx.doi.org/10.1016/j.coastaleng.2009.11.007).

708 Sánchez-Linares, C., 2011. Simulación numérica de tsunamis generados por  
709 avalanchas submarinas: aplicación al caso de Lituya Bay. Master’s thesis.  
710 University of Málaga. Spain.



- 711 Schäffer, H.A., Madsen, P.A., 1995. Further enhancements of Boussinesq-type  
712 equations. *Coastal Engineering* 26, 1 – 14. doi:10.1016/0378-3839(95)  
713 00017-2.
- 714 Watts, P., Grilli, S.T., Kirby, J.T., Fryer, G.J., Tappin, D.R., 2003. Landslide  
715 tsunami case studies using a Boussinesq model and a fully nonlinear tsunami  
716 generation model. *Natural Hazards and Earth System Sciences* 3, 391–402.  
717 doi:10.5194/nhess-3-391-2003.
- 718 Watts, P., Grilli, S.T., Tappin, D.R., Fryer, G.J., 2005. Tsunami generation by  
719 submarine mass failure. II: Predictive equations and case studies. *Journal of*  
720 *Waterway, Port, Coastal, and Ocean Engineering* 131, 298–310. doi:10.1061/  
721 (ASCE)0733-950X(2005)131:6(298).
- 722 Wu, T.R., 2004. A numerical study of three-dimensional breaking waves and  
723 turbulence effects. Ph.D. thesis. Cornell University.